Supplementary Materials

Heteroatom-driven the rapid electrochemical process of anthracite derivatives in sodium-ion battery

Lianli Zou[*], Tongbo Yang, Longwei Li, Ling Lin, Maoxiang Jing, Qiuju Wang[*]

Institute for Advanced Materials, School of Materials Science and Engineering,
Jiangsu University, Zhenjiang 212013, Jiangsu, China.

[*]**Correspondence to**: Dr. Lianli Zou, Dr. Qiuju Wang, Institute for Advanced Materials, School of Materials Science and Engineering, Jiangsu University, Zhenjiang 212013, Jiangsu, China. E-mail: lianli_zou@ujs.edu.cn; wang_qiuju@ujs.edu.cn

Chemicals

In this work, anthracite coal was purchased from Hebei Xiari Group Energy Co., Ltd., China. Hydrochloric acid (HCl, 36%-38%), hydrofluoric acid (HF, ≥ 40%), ammonium chloride (NH_4Cl, ≥ 99.5%), sodium chloride (NaCl, ≥ 99.5%), potassium chloride (KCl, ≥ 99.5%), N-methyl-2-pyrrolidone (NMP, ≥ 99.5%), and anhydrous ethanol (CH_3CH_2OH, ≥ 99.7%) were purchased from Sinopharm Chemical Reagent Co, Ltd., China. Ammonium bromide (NH_4Br, ≥ 99.9%) was supplied from Shanghai Macklin Biochemical Co., Ltd., China. Polyvinylidene fluoride (PVDF, ≥ 99.99%) was purchased from Arkema, France. Sodium tablets (15.6 mm) and sodium-ion battery electrolyte were purchased from CORNEX New Energy Co, Ltd., China. The glass fiber membrane was purchased from Whatman, UK. Carbon-coated aluminum foil was obtained from Shenzhen Kejing Zhida Technology Co., Ltd., China. All the other chemicals were used without further purification. Deionized water was obtained from an AK series water purifier (Chengdu Tangshi Kangning Technology Co., Ltd., China).

According to Bragg's Law:

$$n * \lambda = 2 * d * sin\theta \tag{1}$$

For the (002) reflection of carbon materials, n=1. The interlayer spacing d_{002} is calculated by:

$$d_{(002)} = \frac{\lambda}{2 * sin\theta_{(002)}} \tag{2}$$

In which λ is X-ray wavelength (for Cu Kα radiation, λ=0.15418 nm), θ is Bragg angle (in degrees) corresponding to the (002) peak.

According to the Scherrer formula eq 3, the lateral size (L_a) of carbon layers and the stacking height (L_c) of aromatic layers are calculated.

$$D_{(hkl)} = \frac{K * \lambda}{\beta * \cos(\theta)} \tag{3}$$

in which L_a=$D_{(101)}$, L_C=$D_{(002)}$, K is the shape factor which is most commonly taken as 0.89, λ is wavelength of X-ray (1.54 Å for Cu target), and β is the half width of (hkl).

The detailed calculation process of the $d_{(002)}$, La and L_c is as follows:

The fitting of XRD curves and calculation of $d_{(002)}$, La and L_c were both performed using the software Origin. The baseline was selected in a custom mode, with anchor points added in regions of the curve without characteristic peaks, which is crucial for achieving reproducibility and reliability. The baseline was automatically subtracted, and the baseline-corrected data were used for plotting. Then, Gauss was chosen as the peak function.

The detailed calculation process of the I_D/I_G ratio is as follows:

The fitting and calculation of I_D and I_G were both performed using the software Origin. The baseline was selected in a custom mode, with anchor points added in regions of the curve without characteristic peaks, which is crucial for achieving reproducibility and reliability. The baseline was automatically subtracted, and the baseline-corrected data were used for plotting. The gaussian function was chosen as the peak function.

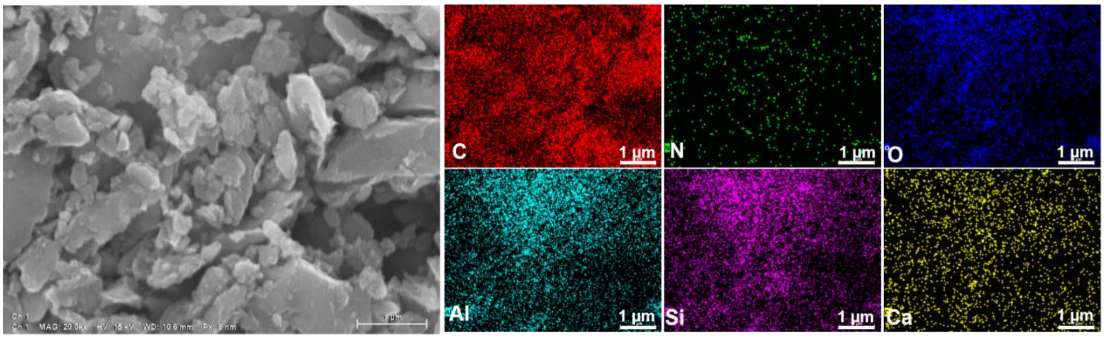

Supplementary Figure 1. SEM and the corresponding mapping images of C.

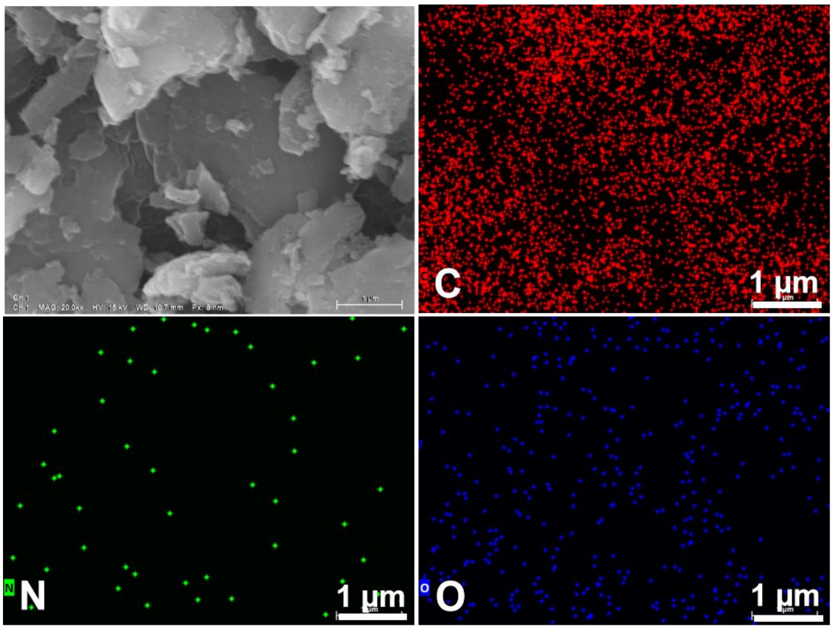

Supplementary Figure 2. SEM and the corresponding mapping images of Cp.

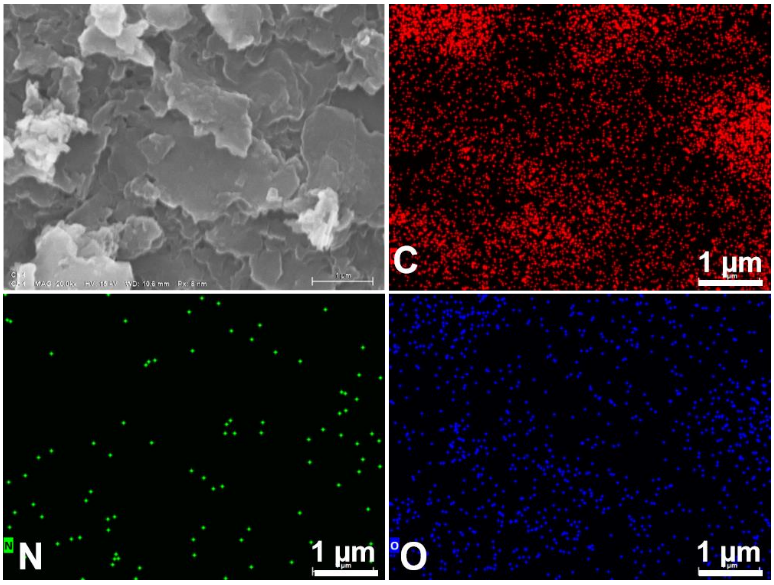

Supplementary Figure 3. SEM and the corresponding mapping images of ACp.

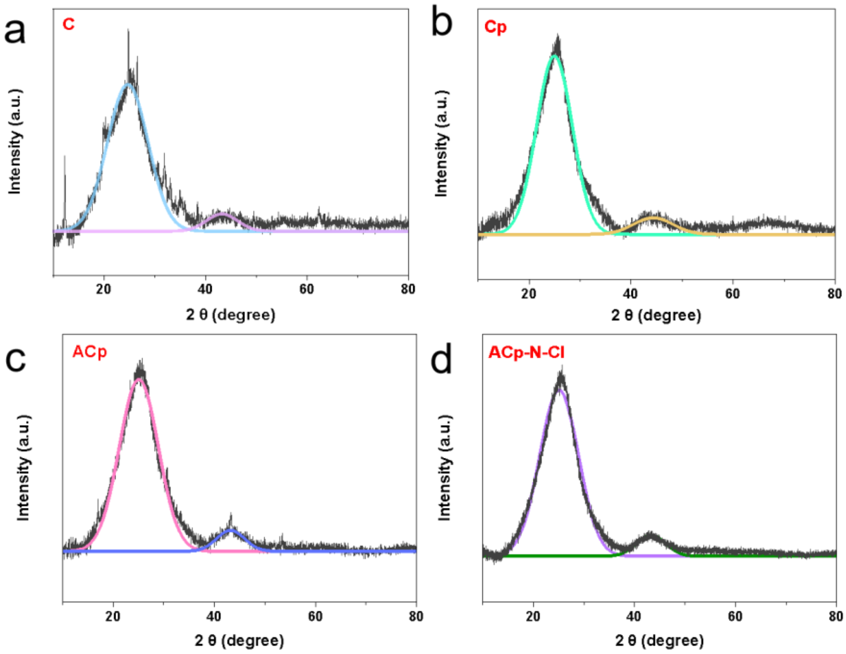

Supplementary Figure 4. Baseline-corrected XRD curves and simulated peaks of (a) C; (b) Cp; (c) ACp and (d) ACp-N-Cl.

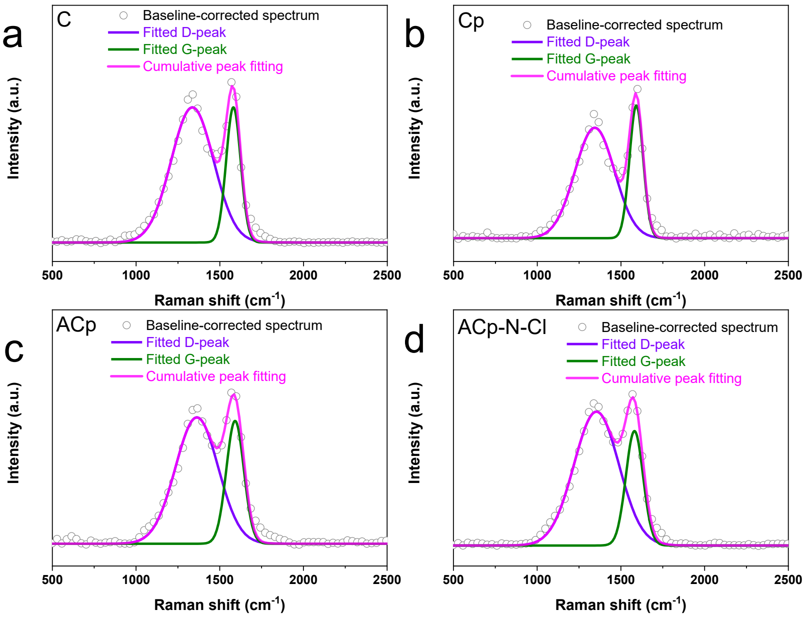

Supplementary Figure 5. Baseline-corrected Raman curves and fitted D and G peaks of (a) C; (b) Cp; (c) ACp and (d) ACp-N-Cl.

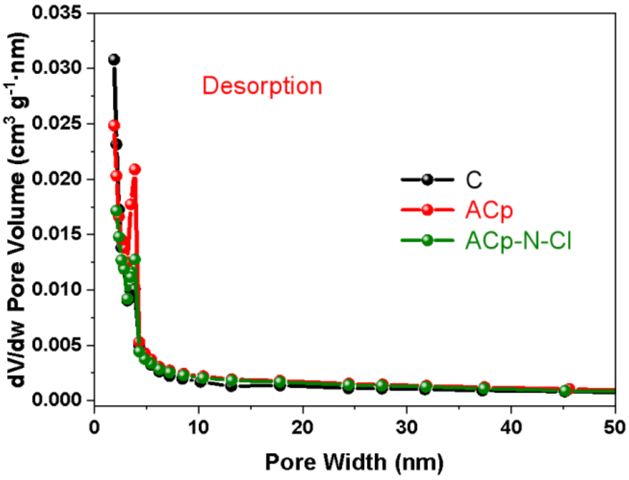

Supplementary Figure 6. The pore size distribution of different samples.

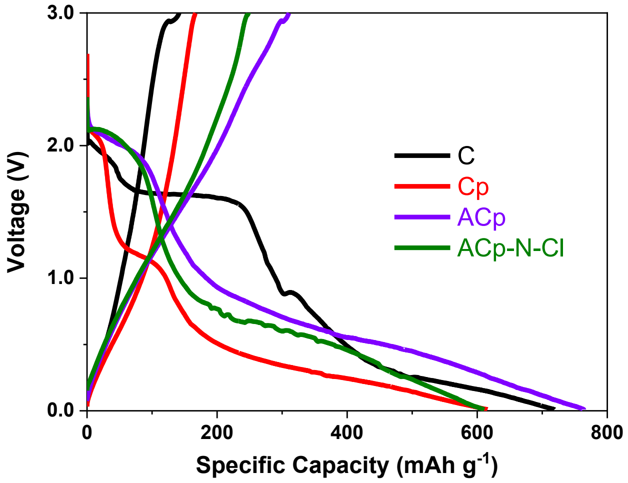

Supplementary Figure 7. The first-round charge-discharge curves at 0.02 A g^{-1} during the activation process.

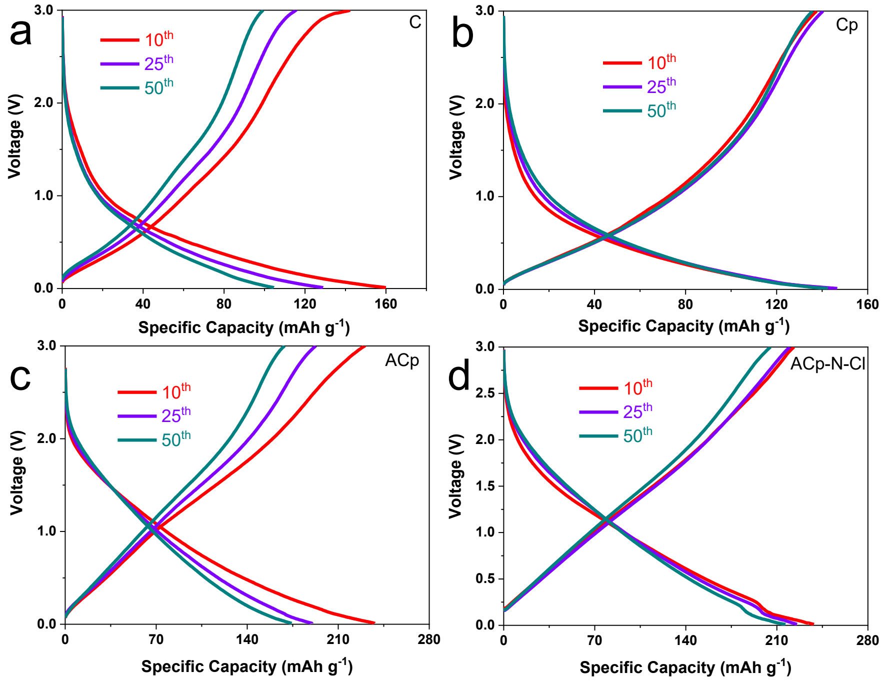

Supplementary Figure 8. Charge-discharge curves of (a) C; (b) Cp; (c) ACp and (d) ACp-N-Cl at different cycle numbers at 0.02 A g^{-1}.

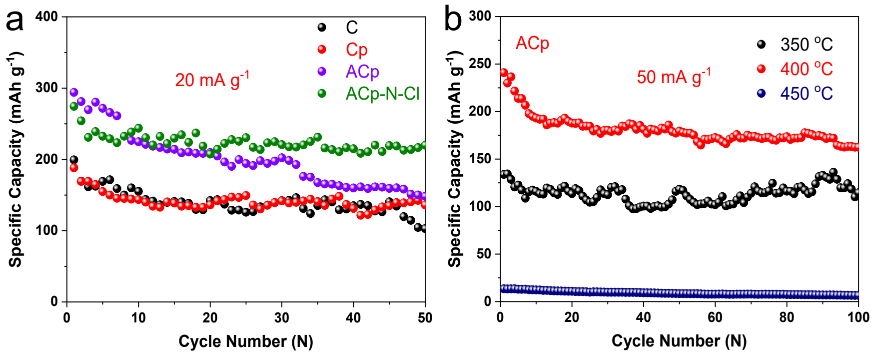

Supplementary Figure 9. (a) The cycling performance of the synthesized samples at a current density of 20m A g^{-1}, (b) the cycling performance of ACp at different temperatures.

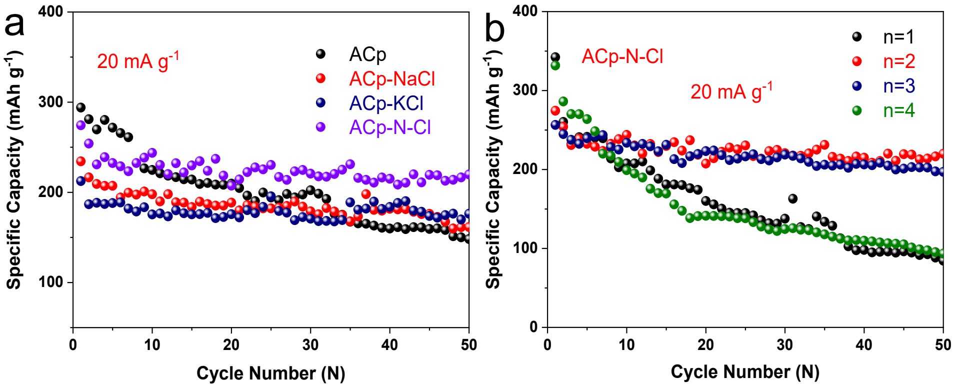

Supplementary Figure 10. (a) The cyclic performance of ACp、ACp-NaCl、ACp-KCl、ACp-N-Cl and (b) ACp with different mass ratios to ammonium chloride (n=m_{ACp}:m_{NH4Cl}).

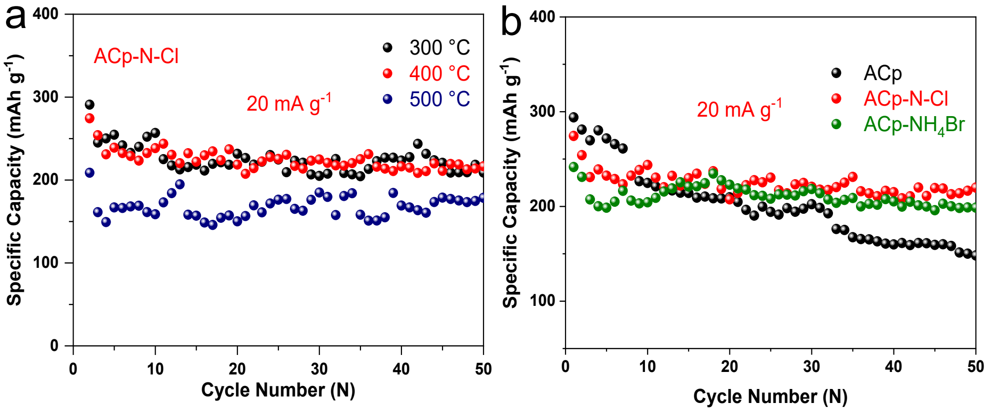

Supplementary Figure 11. (a) The cyclic performance of ACp-N-Cl under different temperatures, (b) comparison of cyclic performances of ACp、ACp-N-Cl and ACp-NH_4Br.

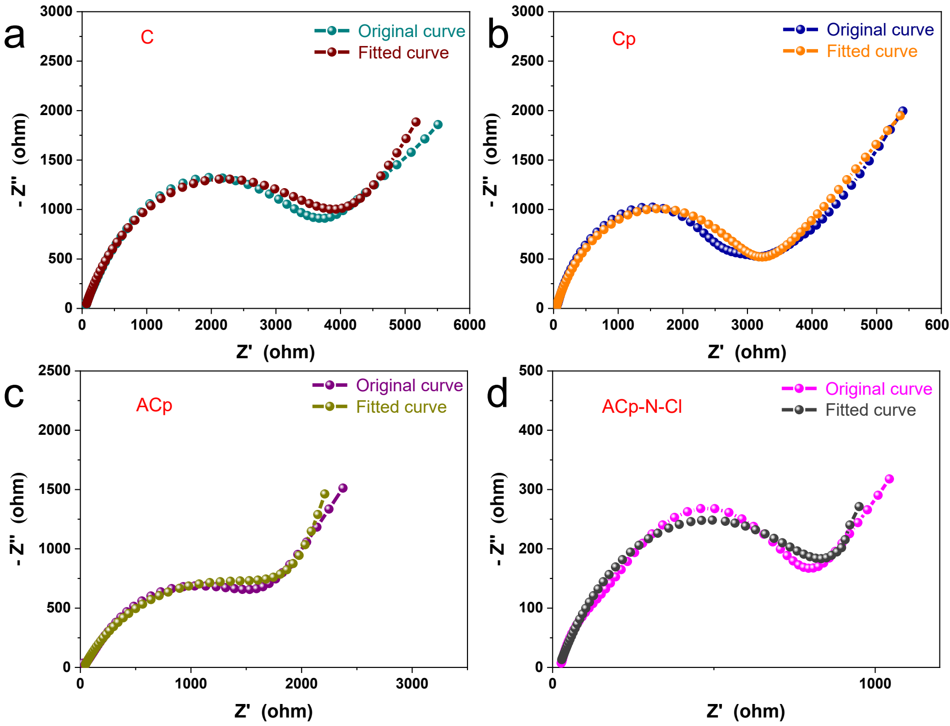

Supplementary Figure 12. EIS results of (a) C, (b) Cp, (c) ACp and (d) ACp-N-Cl with their corresponding fitting curves.

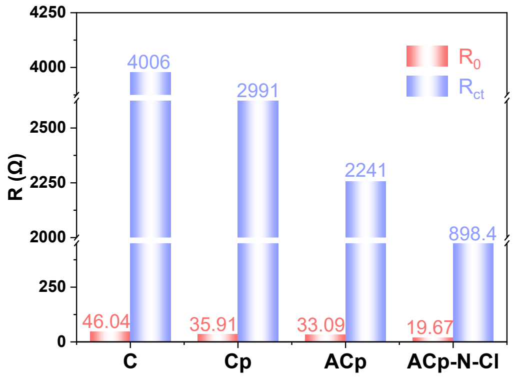

Supplementary Figure 13. The bar chart of the fitted R_0 and R_{ct} values for different samples.

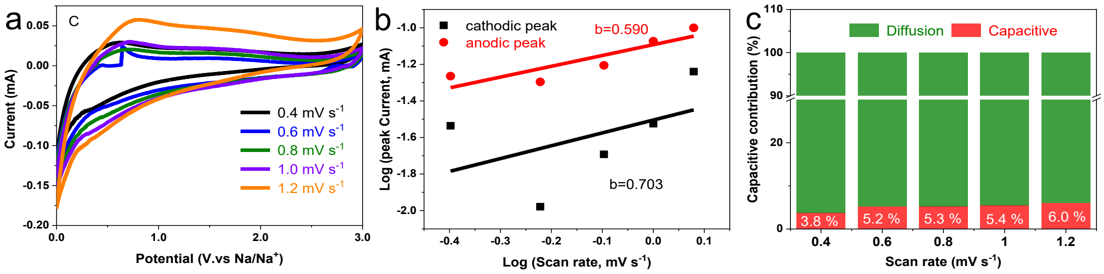

Supplementary Figure 14. CV curves at (a) various scanning rates, (b) b values of C for cathodic and anodic peaks, and (c) percentage of surface capacitance contribution in C at different sweep rates.

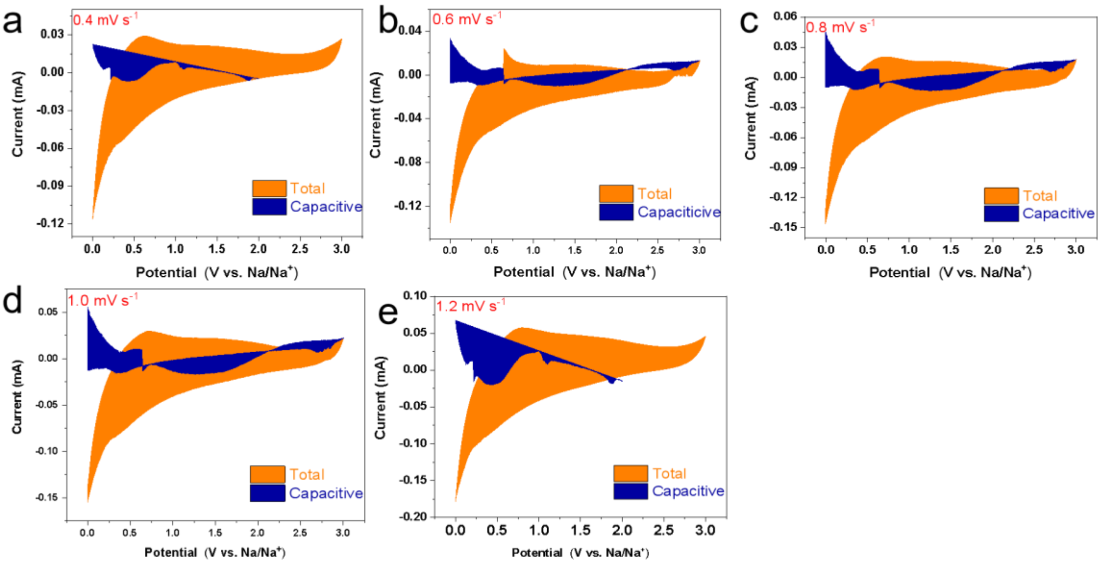

Supplementary Figure 15. The pseudocapacitive contribution of C at different sweep rates (a) 0.4 mV s^{-1}, (b) 0.6 mV s^{-1}, (c) 0.8 mV s^{-1}, (d) 1.0 mV s^{-1}, (e) 1.2 mV s^{-1}.

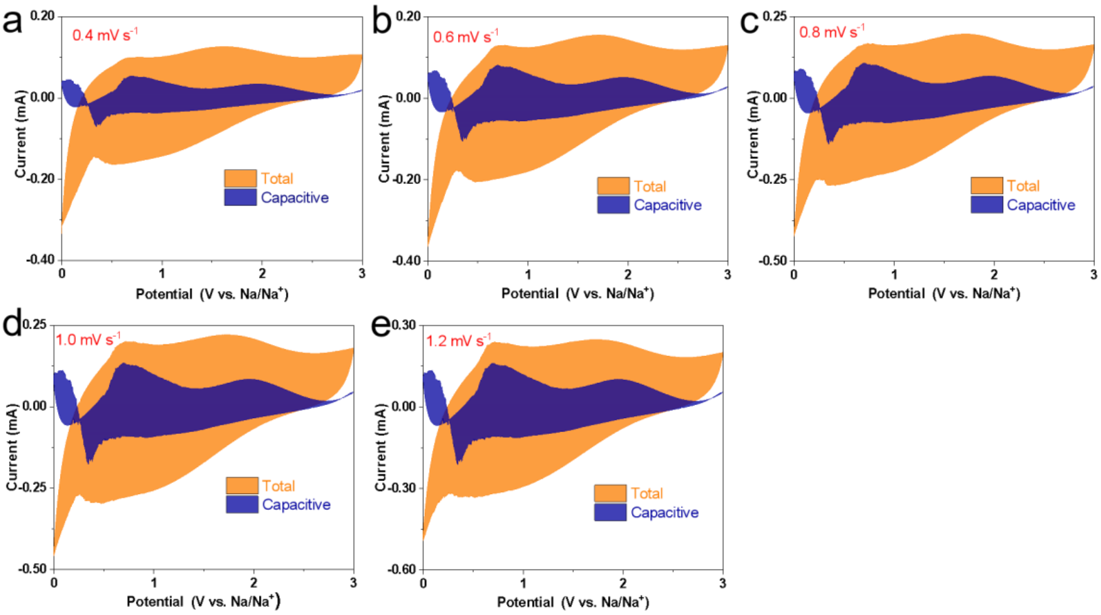

Supplementary Figure 16. The pseudocapacitive contribution of ACp-N-Cl at different sweep rates (a) 0.4 mV s^{-1}, (b) 0.6 mV s^{-1}, (c) 0.8 mV s^{-1}, (d) 1.0 mV s^{-1}, (e) 1.2 mV s^{-1}.

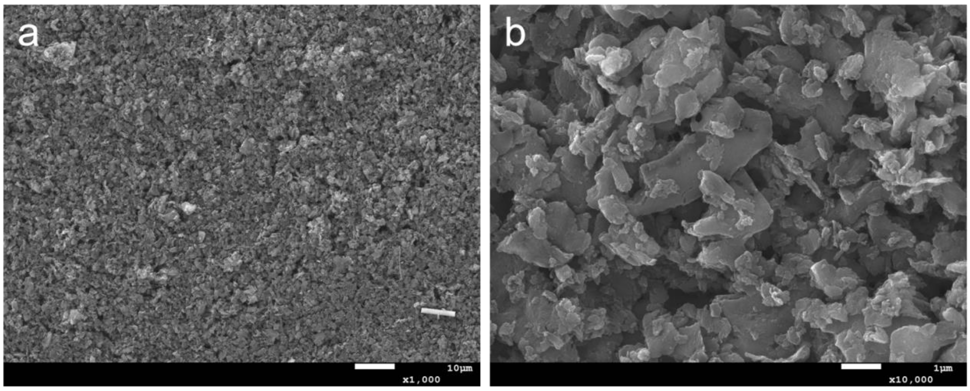

Supplementary Figure 17. SEM images of ACp-N-Cl electrode at different magnifications.

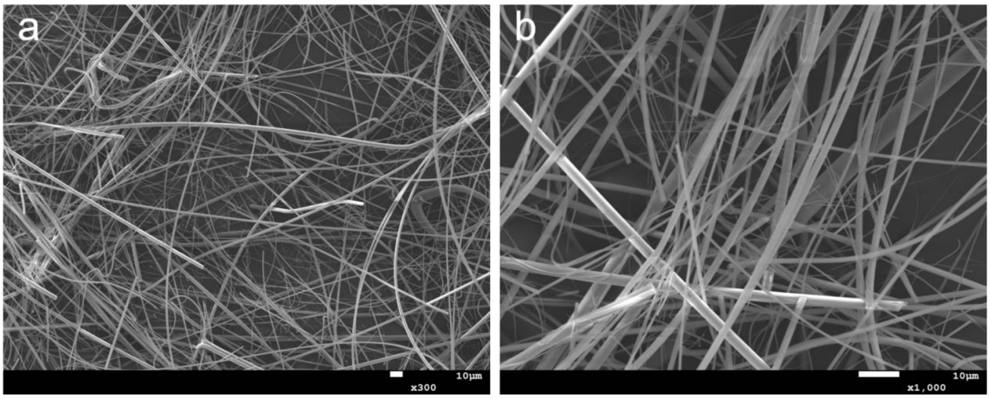

Supplementary Figure 18. SEM images of glass fiber at different magnifications.

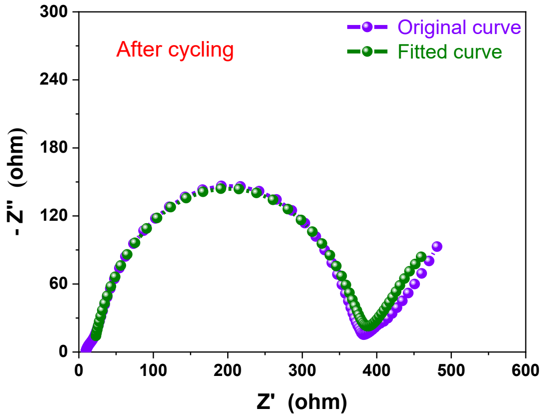

Supplementary Figure 19. EIS result of ACp-N-Cl with the corresponding fitting curve.

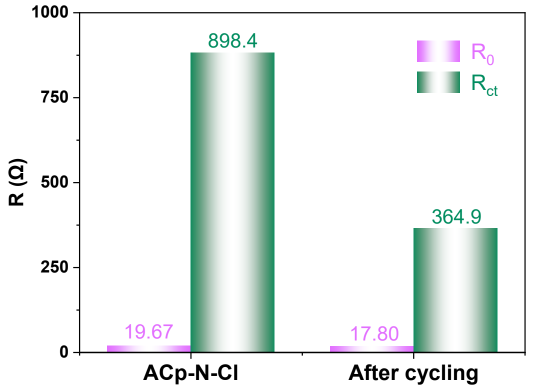

Supplementary Figure 20. The bar chart of the fitted R_0 and R_{ct} values of ACp-N-Cl before and after cycling.

Supplementary Table 1. Summary of instrument names, manufacturers, and manufacturing factories

Instrument Name	**manufacturer, manufacture factory**
Air blast drying oven	Shanghai Yiheng Scientific Instruments Co., Ltd., China
Electronic analytical balance	Suzhou Jinzuan Weighing Equipment Co., Ltd., China
Vacuum drying oven	Hefei Kejing Material Technology Co., Ltd., China
Pipe furnace	Hefei Kejing Material Technology Co., Ltd., China
Muffle furnace	Hefei Kejing Material Technology Co., Ltd., China
X-ray diffractometer	Bruker, Germany
Specific Surface Area Porosity Analyzer	Micromeritics Instrument Corporation, USA
Scanning electron microscope	JEOL Ltd., Japan
Fourier transform infrared spectrometer	Tianjin Port East Technology Co., Ltd., China
Transmission electron microscope	JEOL Ltd., Japan
Raman spectrometer	Thermo Fisher Scientific Inc., USA
X-ray Photoelectron Spectroscopy	Thermo Fisher Scientific Inc., USA

Stirring Defoaming Machine	Guangzhou Schnos Technology Co., Ltd., China
Automatic Coating Machine	Hefei Kejing Materials Technology Co., Ltd., China
Ultra-pure argon gas glove box	Shanghai Mikaelona Electromechanical Technology Co., Ltd., China
Cutting Machine	Sichuang Precision Technology Co., Ltd., China
Button Battery Closure Machine	Shenzhen Kejing Zhida Technology Co., Ltd., China
Electrochemical Workstation	Shanghai Chenhua Instrument Co., Ltd., China
Constant Current Charging and Discharging Equipment	Wuhan Landian Electronics Co., Ltd., China

Supplementary Table 2. Detailed EDS elemental analysis in atomic % of (a) C、(b) Cp ,(c) ACp and (d) ACp-N-Cl

Sample	C	N	O	Cl	Al	Si	Ca
C	90.40	1.82	6.41	0	0.66	0.69	0.02
Cp	94.66	2.02	3.32	0	0	0	0
ACp	76.33	1.73	21.94	0	0	0	0
ACp-N-Cl	70.81	15.96	13.20	0.03	0	0	0

Supplementary Table 3. Parameters calculated from the fitted XRD results of different samples

Sample	d_{002} (nm)	γ	FWHM	L_c (nm)	L_a (nm)
C	0.36	24.76°/43.29°	9.44/7.22	0.85	2.42
Cp	0.36	24.92°/43.98°	9.74/6.77	0.82	2.58
ACp	0.35	25.07°/43.21°	9.11/6.54	0.88	2.67
ACp-N-Cl	0.35	24.93°/43.79°	9.80/7.3	0.76	2.23

Supplementary Table 4. Parameters calculated from the fitted Raman results of different samples

Samples	Peak types	Fitted peak area	FWHM	Peak height	Center of mass	$I_D/I_G=A_D/A_G$

C	Fitted D-peak (Gaussian)	226.68	299.07	0.71	1336.18	2.92
	Fitted G-peak (Gaussian)	77.51	102.24	0.71	1580.90	
Cp	Fitted D-peak (Gaussian)	140.70	278.78	0.47	1343.51	2.42
	Fitted G-peak (Gaussian)	58.15	95.95	0.57	1591.69	
ACp	Fitted D-peak (Gaussian)	181.05	299.94	0.57	1363.40	2.51
	Fitted G-peak (Gaussian)	72.19	123.06	0.55	1591.68	
ACp-N-Cl	Fitted D-peak (Gaussian)	219.33	315.47	0.65	1354.19	3.04
	Fitted G-peak (Gaussian)	72.09	121.32	0.56	1581.19	

Supplementary Table 5. The BET surface area, pore volume and average pore size of C, ACp and ACp-N-Cl

Samples	**S_{BET} (m^2 g^{-1})**	**Pore volume (cm^3 g^{-1})**	**Average pore size (nm)**
C	317.39	0.13	6.85
ACp	339.57	0.16	7.71
ACp-N-Cl	265.90	0.14	8.06

Supplementary Table 6. First charge-discharge data and initial coulombic efficiency at 0.02 A g^{-1} during the activation process of different samples

Sample	**First discharge (mAh g^{-1})**	**First charge (mAh g^{-1})**	**Coulombic efficiency (%)**
C	718.80	141.65	19.71
Cp	615.66	166.57	27.06
ACp	763.93	310.44	40.58

ACp-N-Cl	610.82	248.34	40.66

Supplementary Table 7. Detailed fitting EIS results of C, Cp, ACp and ACp-N-Cl

Samples **Element**	**C**	**Cp**	**ACp**	**ACp-N-Cl**
R_0	46.04	35.91	33.09	19.67
R_{ct}	4006.00	2991.00	2241.00	898.40
W_0-R	23940.00	12845.00	131.40	829.60
W_0-T	9.45	426.60	$2.83 * 10^{-3}$	0.36
W_0-P	0.58	0.44	0.42	0.71
CPE-T	$2.39 * 10^{-6}$	$8.60 * 10^{-6}$	$7.51 * 10^{-6}$	$1.48 * 10^{-5}$
CPE-P	0.71	0.73	0.69	0.63

Supplementary Table 8. Detailed fitting EIS results of the ACp-N-Cl after cycling

	Elements	**Value**
ACp-N-Cl after cycling	R_0	17.80
	R_{ct}	364.90
	W_0-R	335.70
	W_0-T	73.77
	W_0-P	0.56
	CPE-T	$2.92 * 10^{-5}$
	CPE-P	0.84